



Transparent, Ultrahigh-Gas-Barrier Films with a Brick–Mortar–Sand Structure**

Yibo Dou, Ting Pan, Simin Xu, Hong Yan, Jingbin Han,* Min Wei,* David G. Evans, and Xue Duan

Abstract: Transparent and flexible gas-barrier materials have shown broad applications in electronics, food, and pharmaceutical preservation. Herein, we report ultrahigh-gas-barrier films with a brick–mortar–sand structure fabricated by layer-by-layer (LBL) assembly of XAl-layered double hydroxide (LDH, X = Mg, Ni, Zn, Co) nanoplatelets and polyacrylic acid (PAA) followed by CO₂ infilling, denoted as (XAl-LDH/PAA)_n-CO₂. The near-perfectly parallel orientation of the LDH “brick” creates a long diffusion length to hinder the transmission of gas molecules in the PAA “mortar”. Most significantly, both the experimental studies and theoretical simulations reveal that the chemically adsorbed CO₂ acts like “sand” to fill the free volume at the organic–inorganic interface, which further depresses the diffusion of permeating gas. The strategy presented here provides a new insight into the perception of barrier mechanism, and the (XAl-LDH/PAA)_n-CO₂ film is among the best gas barrier films ever reported.

Reactive gases cause food decomposition and electrical cutting-out in electronic devices, thus in the food/pharmaceutical packaging and electronic encapsulation industries a low oxygen-transmission rate (O₂TR) is the key issue.^[1–3] Therefore, innovative developments of barrier materials with low gas permeability produced by environment-friendly processes are highly desired.^[4,5] Conventional organic–inorganic composites have been constructed by filling inorganic nanoplatelets, such as clay, silicon oxide, and graphene, into a polymer matrix to generate a “brick–mortar” structure with an extended diffusion path for permeating gas molecules.^[6–8] Despite considerable research, perceptions of the barrier mechanism are still limited to the “tortuous theories”

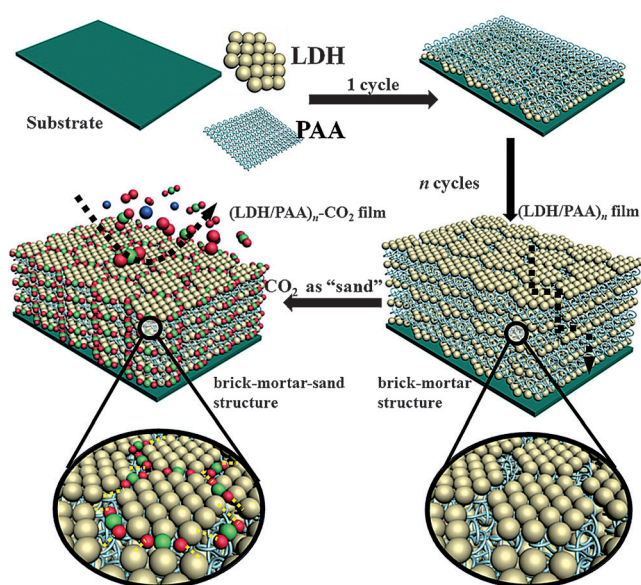
proposed in the last century.^[9,10] These theories propose that the aspect ratio (A_R) of inorganic platelet is an essential parameter for an organic–inorganic gas-barrier film; that is, a higher A_R normally induces better barrier properties. Based on this consensus, inorganic platelets with large A_R were employed to fabricate brick–mortar structures with low gas permeability. However, an excessive pursuit of high A_R generally results in low toughness and homogeneity for barrier films, which ultimately restricts their practical applications. In addition, the free volume is another key parameter for barrier films, as a higher fraction of free volume enables the gas molecules to diffuse across the films in a more convenient way. Since the free volume is generated by surface incompatibility between polymeric and inorganic components, it can hardly be eliminated in a brick–mortar structure, even with elaborate design.^[11] Therefore, it is still a challenge to develop novel approaches to obtain new barrier materials which can resolve these problems and still have gas-barrier properties.

Recent advances in ordered organic–inorganic materials have revealed the two dimensional (2D) nanostructure imparts composites with specific mechanical, physicochemical, and optical properties.^[12,13] Layered double hydroxides (LDHs) are one type of important 2D layered materials, whose structure can be generally expressed as $[M^{II}_{1-x}M^{III}_x(OH)_2](A^{n-})_{x/n} \cdot mH_2O$ (M^{II} and M^{III} are divalent and trivalent metals, respectively, A^{n-} is interlayered anion).^[14–17] In our previous work, LDHs-based functional materials have been investigated in the fields of biology, barriers, and electrochemistry.^[18,19] In addition, owing to the abundant density of surface basic sites, LDH materials have displayed strong adsorption capabilities for acidic gases (e.g., CO₂, SO_x, and NO_x).^[20,21] Based on the unique nature of LDH nanoplatelets, a three-component hybrid structure constructed from LDH, polymer matrix, and acid gas molecules could be an effective strategy to achieve excellent gas-barrier films. Herein, we fabricate ultrahigh-gas-barrier films with a brick–mortar–sand structure by the alternating assembly of XAl-LDH nanoplatelets (X = Mg, Ni, Zn, Co) and polyacrylic acid (PAA) and subsequent CO₂ adsorption (Scheme 1). The resultant (XAl-LDH/PAA)_n-CO₂ films has the following advantages: firstly, 2D LDH nanoplatelets combined with polymer in a brick–mortar structure suppress the permeability of gas molecules, as a result of the increased diffusion length and strong diffusion resistance; secondly, CO₂ molecules as “sand” can be immobilized on the LDH surface to form a brick–mortar–sand structure, the “sand” fills the free volume and further improves the gas-barrier behavior.

[*] Y. Dou, T. Pan, S. Xu, Dr. H. Yan, Dr. J. Han, Prof. M. Wei, Prof. D. G. Evans, Prof. X. Duan
 State Key Laboratory of Chemical Resource Engineering
 Beijing University of Chemical Technology
 15 Beisanhuan East Road, Beijing 100029 (China)
 E-mail: hanjb@mail.buct.edu.cn
 weimin@mail.buct.edu.cn

[**] This work was supported by the 973 Program (Grant No. 2014CB932104), the National Natural Science Foundation of China (NSFC), and the Beijing Natural Science Foundation (2132043). M.W. particularly appreciates the financial aid from the China National Funds for Distinguished Young Scientists of the NSFC. We acknowledge the National Supercomputing Center in Shenzhen for providing the computational resources and materials studio (version 6.1, CASTEP and Forcite module).

Supporting information for this article (including preparative details and characterization) is available on the WWW under <http://dx.doi.org/10.1002/anie.201503797>.



Scheme 1. Schematic illustration for the fabrication of (XAl-LDH/PAA)_n-CO₂ barrier films with a brick-mortar-sand structure green C, red O. Broken black line indicates the gas-diffusion path in the brick-mortar structure.

XAl-LDH ($X = \text{Mg, Ni, Zn, and Co}$) samples with high crystallinity were synthesized by the separate nucleation and aging steps method reported by our group.^[22,23] Figure 1A shows the XRD patterns of these XAl-LDH samples, which can be indexed as a nitrate-containing hexagonal structure with $2\theta = 11.2^\circ, 22.5^\circ, 33.8^\circ, 37.5^\circ,$ and 61.1° ($d_{003} = 7.89, d_{006} = 3.97, d_{009} = 2.66, d_{012} = 2.40,$ and $d_{110} = 1.51 \text{ \AA}$). No other crystalline phase is detected, indicating the high purity of the products. SEM images and particle size analysis (Figures S1 and S2 in the Supporting Information) display a narrow size distribution for the individual hexagonal XAl-LDH nanoplatelets (60–110 nm). In addition, the N₂-adsorption/desorption measurements reveal typical type IV isotherms with H3-type hysteresis loops ($P/P_0 > 0.4$) for all the LDH samples; and their specific surface area ranges in 73.8–135.2 m² g⁻¹ (Figure S3).

To further investigate their ability to adsorb acid gas, CO₂ temperature programmed desorption (TPD) was applied to measure the basic sites in XAl-LDH nanoplatelets. The TPD profiles (Figure 1B) show a series of strong desorption peaks, indicating the presence of abundant basic sites in these LDH samples. Their basic sites can be classified into three categories: weak (105–140°C: attributed to bicarbonate species released from OH⁻ groups), middle (140–175°C: assigned to bidentate carbonates desorbed from X-O pairs), and strong (175–215°C: owing to unidentate carbonates released from low-coordination O²⁻ anions related to the crystal defects).^[20] From the integral areas of TPD spectra, MgAl-LDH exhibits the largest adsorption capacity for CO₂ gas in contrast to other samples. Moreover, in situ infrared spectroscopy is applied as a supplementary technique to further confirm the chemical adsorption of CO₂ on XAl-LDH samples.^[24,25] Figure 1C–F show in situ infrared spectra obtained over these XAl-LDH samples after CO₂ adsorption

at 20°C and sequential evaluations at 120 and 200°C. Three broad infrared bands are observed at 20°C, which are attributed to the superimposition of unidentate carbonate (1510–1560 cm⁻¹), bidentate carbonate (1360–1380 and 1290–1330 cm⁻¹), and bicarbonate (1640–1650, 1480–1490, and 1270–1280 cm⁻¹). As the temperature increases from 20 to 200°C, the intensity of absorption bands decreases gradually, demonstrating the desorption of CO₂ from LDH. The CO₂ TPD combined with in situ infrared spectra indicate the XAl-LDH nanoplatelets have three kinds of basic sites (especially for MgAl-LDH with more strong-basic sites), accounting for a high CO₂ adsorption capability. This situation favors the bonding of CO₂ as “sand” for the construction of the brick-mortar-sand structure.

The well-dispersed LDH suspensions display clear Tyndall light scattering phenomenon (Figure S4), the suspensions were used to fabricate (LDH/PAA)_n films by the layer-by-layer (LBL) assembly method. The assembly process is monitored by UV/Vis absorption and the (LDH/PAA)_n films exhibit a strong band at 193 nm attributed to the characteristic absorption of PAA (Figure 2A and Figure S5). The absorption intensity gradually becomes stronger with the increase of bilayer number n , indicating a stepwise and regular deposition procedure. In addition, the X-ray photoelectron spectroscopy (XPS) results demonstrate that the assembly process is driven by electrostatic interactions between the negatively charged PAA and the positively charged LDH (Figure S6–S9; see details in the Supporting Information).

The structural details of as-prepared (XAl-LDH/PAA)₁₅ films are measured by X-ray diffraction XRD (Figure 2B and Figure S10), which only display the (003) reflection of LDH phase ($2\theta \approx 11.2^\circ$) and the amorphous diffraction of PET substrate ($2\theta \approx 23.2^\circ$). The absence of any nonbasal reflections ($h, l \neq 0$) compared with LDH powdered samples (Figure 1A) verifies the preferred orientation of LDH nanoplatelets with the ab plane parallel to the substrate, indicating the formation of a brick-mortar structure. The thickness and surface morphology of (XAl-LDH/PAA)₁₅ films were further investigated by SEM and AFM observations. The top-view SEM images display densely packed LDH nanoplatelets on the smooth surface (Figure 2C and Figure S11); the side-view SEM images (Figure 2C, inset) reveal a thickness of approximately 149 nm. Furthermore, energy dispersive X-ray spectroscopy (EDX) mapping analysis for (MgAl-LDH/PAA)₁₅ film (Figure 2D) shows that Mg, Al, O, and C are homogeneously distributed throughout the film. AFM images reveal that the value of root-mean-square (rms) roughness ranges in 13.5–15.4 nm for these (XAl-LDH/PAA)₁₅ films (Figure 2E and Figure S12), which is lower than those of reported barrier films,^[26,27] demonstrating a relatively uniform surface. In addition, the homogeneous distribution and orientation of LDH nanoplatelets impart the (XAl-LDH/PAA)₁₅ films on PET substrates a remarkable transparency, with an average light transmittance of approximately 80% across the visible-light spectrum (Figures S13, S14).

Free volume is an important parameter to evaluate the permeability of barrier materials,^[28] which was measured by the positron annihilation technique based on positron lifetime

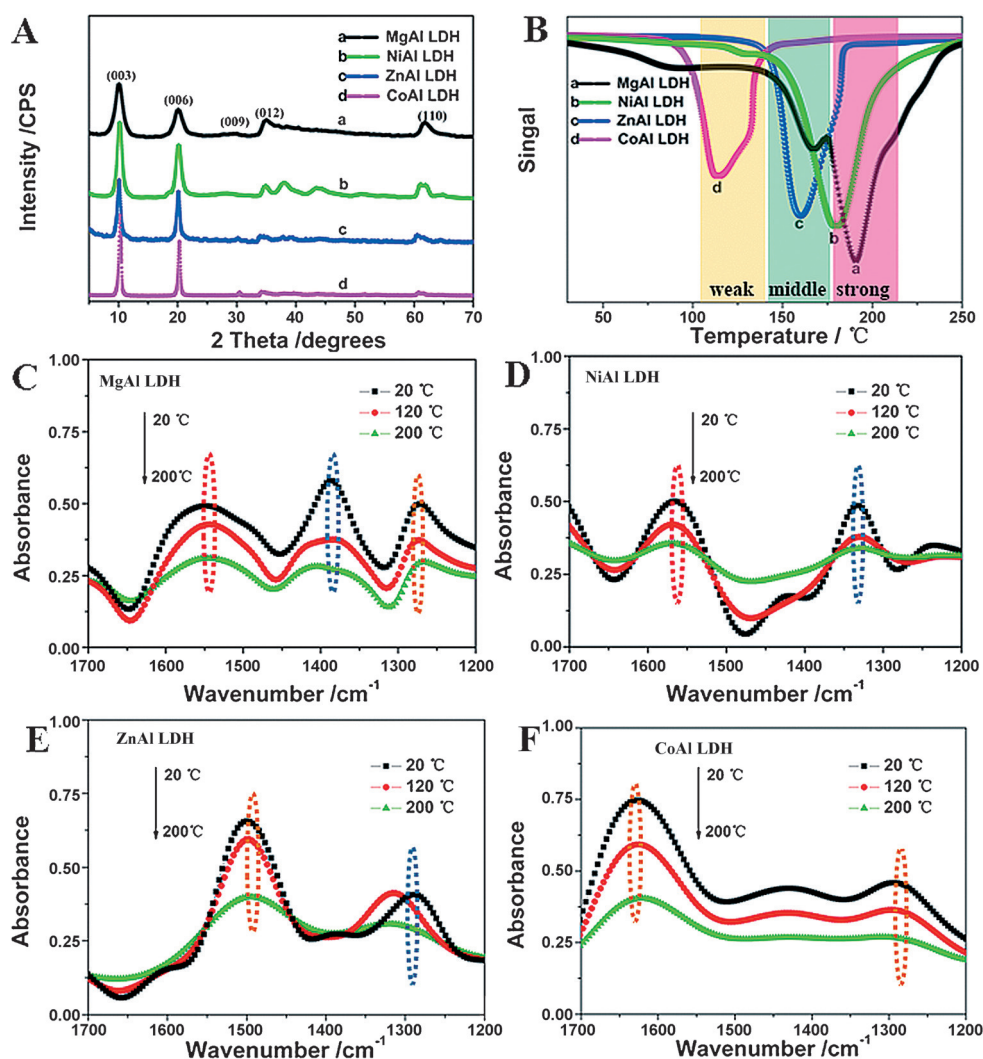


Figure 1. A) XRD patterns, B) CO₂ TPD profiles for XAl-LDH nanoplatelets (X: a) Mg, b) Ni, c) Zn, and d) Co; see text for details), and in situ infrared spectra for C) MgAl, D) NiAl, E) ZnAl, and F) CoAl-LDH samples (red broken circle: unidentate carbonate; blue broken circle: bidentate carbonates; orange broken circle: bicarbonates).

component (τ_3) as well as relative intensity (I_3) (Figure S15, S16: see details in the Supporting Information). Figure 2F shows the free-volume fraction (F_v) of pristine PET and four kinds of (XAl-LDH/PAA)₁₅ films, respectively. For the PET substrate, the free volume fraction is 14.1%. After fabrication of (XAl-LDH/PAA)₁₅ films, the F_v decreases to approximately 11.6%, illustrating the incorporated LDH nanoplatelets reduces F_v by depressing the free slide of polymer chains. Moreover, a further reduction of F_v was observed after CO₂ treatment, owing to the infilling of CO₂ molecules as “sand” in the free space of the existing brick–mortar structure. The (MgAl-LDH/PAA)₁₅-CO₂ film displays the lowest minimum F_v (9.89%) among these four films, as a result of it having the largest adsorption capacity of CO₂. The adsorption of CO₂ molecules onto LDH nanoplatelets plays an important role in reducing the free volume of (LDH/PAA)_n films, which further improves the gas-barrier property.

The barrier properties of various (XAl-LDH/PAA)_n films coated on PET substrates were investigated by oxygen transmission rate (O₂TR) measurements. In contrast to the O₂TR value of 8.372 cm³m⁻²day⁻¹atm⁻¹ for pristine PET substrate, the value for (XAl-LDH/PAA)_n films decreases from around 5.500 to approximately

0.150 cm³m⁻²day⁻¹atm⁻¹ upon increasing n from 5 to 15 (Figure 3A–D). A further decrease to 0.007, 0.024, 0.071, and 0.091 cm³m⁻²day⁻¹atm⁻¹ was observed for CO₂ treated (XAl-LDH/PAA)_n films for X = Mg, Ni, Zn and Co, respectively. It should be noted that the (MgAl-LDH/PAA)_n-CO₂ films in this work show one of the biggest barrier-improvement factors (BIF) among the reported barrier films (Figure S17: see details in the Supporting information). Compared with (XAl-LDH/PAA)₁₅ films, the organic (PDDA/PAA)₆₀ film with similar thickness (ca. 150 nm) displays an inferior oxygen-barrier property (O₂TR = 5.183 cm³m⁻²day⁻¹atm⁻¹; Figure S18). In addition, after CO₂ treatment, the

O₂TR value of (PDDA/PAA)₆₀ film does not exhibit an obvious decrease. The results indicate the 2D LDH bricks create an extreme extension in the diffusion path for oxygen molecules; while the chemically adsorbed CO₂ molecules reduce the free volume of (XAl-LDH/PAA)_n films. This synergistic effect results in the ultrahigh oxygen-barrier property of (XAl-LDH/PAA)_n-CO₂ films.

The O₂ permeability of (MgAl-LDH/PAA)_n-CO₂/PET films can be tuned reversibly by desorption and re-adsorption of CO₂ molecules, which was achieved by nitrogen purging at 150 °C and CO₂ purging at 30 °C, respectively. As shown in Figure S19, along with the CO₂ adsorption–desorption for five cycles, the O₂TR value of (MgAl-LDH/PAA)_n-CO₂/PET film undergoes a reversible variation between around 0.120 and approximately 0.007 cm³m⁻²day⁻¹atm⁻¹. The film stability against water molecules was studied. At room temperature, the immersion of (MgAl-LDH/PAA)₁₅-CO₂/PET film (10 × 10 cm) into water (50 mL) for four weeks did not result in

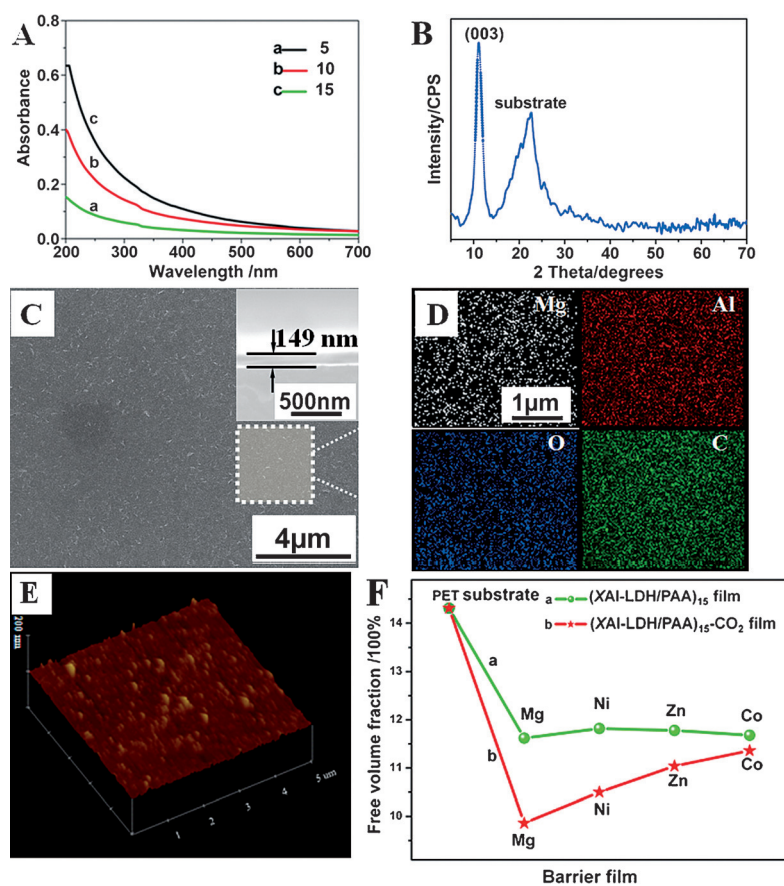


Figure 2. A) UV/Vis spectra of (MgAl-LDH/PAA)_n (n = 5, 10, and 15) films on quartz glass substrates. B) XRD pattern, C) Top-view SEM image (inset: side-view image), D) EDX mapping of the area highlighted in (C), E) AFM image of the (MgAl-LDH/PAA)₁₅ film. F) Free-volume fraction for PET substrate, (XAl-LDH/PAA)₁₅ and (XAl-LDH/PAA)₁₅-CO₂ films coated on PET, respectively. Solid lines are to guide the eye.

a distinct pH variation (Figure S20). Moreover, both the O₂TR value (Figure S21) and visible-light transmittance (Figure S22) of the (MgAl-LDH/PAA)₁₅-CO₂/PET film did not show an obvious change after storage in 85% relative humidity for four weeks. The results indicate the high stability of (MgAl-LDH/PAA)₁₅-CO₂/PET film as a gas-barrier material. To further demonstrate the feasibility of using (MgAl-LDH/PAA)₁₅-CO₂/PET films in food packaging, it was used to protect freshly squeezed orange juice from oxidation (Figure S23; see details in the Supporting Information). The results show that the oxidation of ascorbic acid in orange juice is dramatically depressed when packed in the (MgAl-LDH/PAA)₁₅-CO₂/PET film, a result of the films ultralow oxygen permeability.

In addition to oxygen molecules, the barrier properties of the (MgAl-LDH/PAA)₁₅-CO₂ film towards other gases including CO₂ and He were also studied (Figure 3E,F). The pristine PET substrate shows a larger CO₂TR (37.452 cm³m⁻²day⁻¹atm⁻¹) than O₂TR (8.372 cm³m⁻²day⁻¹atm⁻¹), owing to the different kinetic diameters of CO₂ (0.330 nm) and O₂ (0.346 nm). However, the CO₂TR of (MgAl-LDH/PAA)₁₅-CO₂ film coated on PET

(0.005 cm³m⁻²day⁻¹atm⁻¹) is smaller than its O₂TR (0.007 cm³m⁻²day⁻¹atm⁻¹) value, possibly due to the viscous effect of MgAl-LDH nanoplatelets toward CO₂. In addition, the (MgAl-LDH/PAA)₁₅ film coated on PET displays helium gas-barrier behavior with HeTR = 158.123 cm³m⁻²day⁻¹atm⁻¹ in comparison with PET substrate (HeTR = 233.142 cm³m⁻²day⁻¹atm⁻¹). Similarly, the transmission rate of helium dramatically decreases to 100.274 cm³m⁻²day⁻¹atm⁻¹ after treatment of the film with CO₂, further illustrating the filling of “sand” to brick–mortar structure can also inhibit the diffusion of small gas molecule.

Molecular dynamics (MD) simulations were carried out to give a theoretical insight into the adsorption behavior of CO₂ in the (MgAl-LDH/PAA)_n system and the permeation of O₂ across the (MgAl-LDH/PAA)_n-CO₂ film. The optimized geometry of MgAl-LDH/PAA model is shown in Figure 4A. The binding energy between PAA and MgAl-LDH was calculated to be as high as -4.5 eV per PAA monomer based on first-principle calculations, indicating the existence of electrostatic force in this system, which is in accordance with the XPS experimental results (Figure S6). Density functional theory (DFT) simulations were performed to investi-

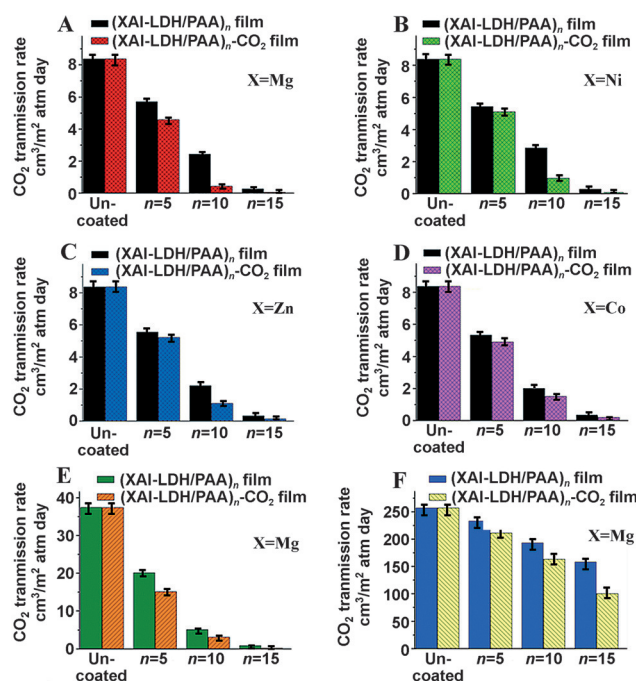


Figure 3. O₂TR values for pristine PET (uncoated), (XAl-LDH/PAA)₁₅ and (XAl-LDH/PAA)₁₅-CO₂ films (X: A-Mg, B-Ni, C-Zn and D-Co) coated on PET substrate. E) CO₂TR and F) HeTR values for pristine PET, (MgAl-LDH/PAA)₁₅ and (MgAl-LDH/PAA)₁₅-CO₂ films coated on PET substrate.

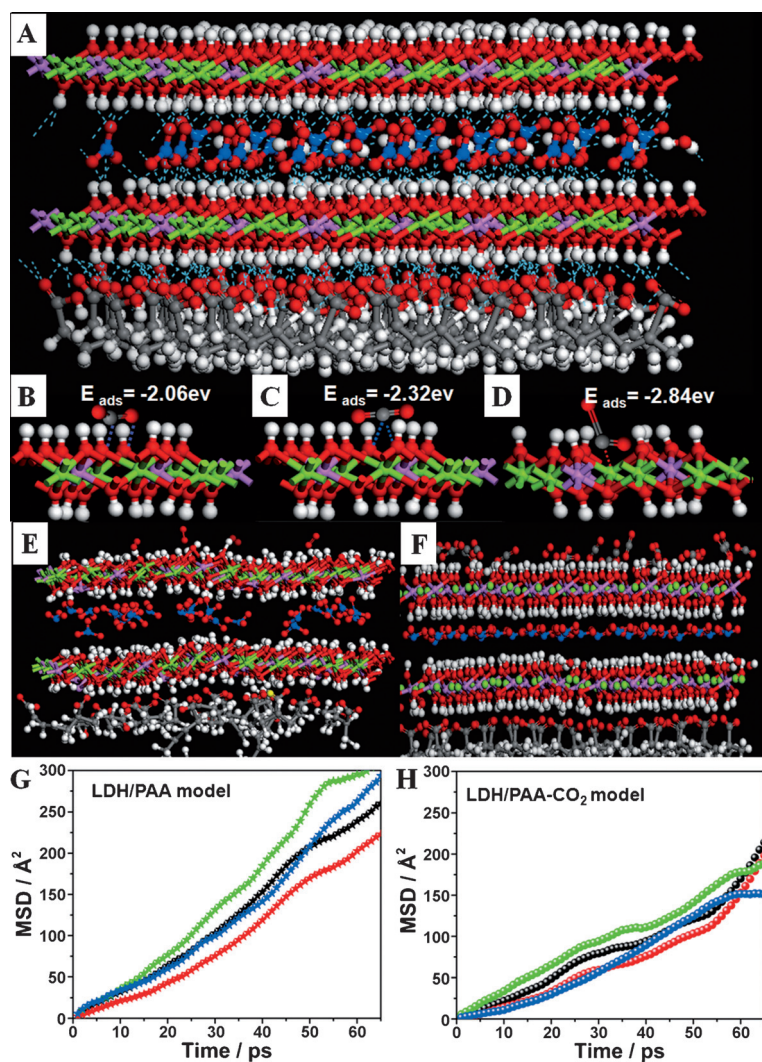


Figure 4. A) The optimized geometry of MgAl-LDH/PAA model (white H, red O, pink Al, green Mg, gray C, blue N). B)–D) The optimized geometries of CO₂ adsorbed on various basic sites of LDH/PAA system. E), F) The optimized geometries of LDH/PAA and (LDH/PAA)-CO₂ model for O₂ diffusion. G), H) The mean squared displacement of four O₂ molecules in LDH/PAA and (LDH/PAA)-CO₂ system within 65 ps (each curve corresponds to one O₂ molecule).

gate the adsorption behavior of CO₂ in the LDH/PAA system by calculating the adsorption energy of CO₂ (E_{ads}) on different adsorption sites through Equation (1):

$$E_{\text{ads}} = E_{(\text{LDH/PAA})-\text{CO}_2} - E_{\text{LDH/PAA}} - E_{\text{CO}_2} \quad (1)$$

where $E_{(\text{LDH/PAA})-\text{CO}_2}$, $E_{\text{LDH/PAA}}$ and E_{CO_2} are the energy of (LDH/PAA)-CO₂, LDH/PAA, and CO₂, respectively. It is found that CO₂ is strongly adsorbed on the three kinds of basic sites in the form of bicarbonate, bidentate carbonate, and unidentate carbonate species, with E_{ads} of -2.06 , -2.32 , and -2.84 eV, respectively (Figure 4B,C and D). The results illustrate the presence of a strong adhesive attraction between CO₂ and LDH/PAA owing to the abundance of basic sites on LDH nanoplatelets.

To better understand the effect of CO₂ adsorption on the barrier properties of the LDH/PAA system, the diffusion coefficients of O₂ molecules on the surface of the LDH/PAA and LDH/PAA-CO₂ systems were calculated by MD simulations (Figure 4E,F). Based on the mean squared displacement (MSD) of O₂ in LDH/PAA and (LDH/PAA)-CO₂ (Figure 4G,H), the diffusion coefficient (D) of O₂ was obtained according to Equation (2):

$$D = \lim_{t \rightarrow \infty} \frac{[r(0) - r(t)]^2}{t} \quad (2)$$

where t is the time; the term in parentheses is MSD. The average diffusion coefficient of O₂ (based on four O₂ molecules) is calculated to be $7.35 \times 10^{-5} \text{ cm}^2 \text{ s}^{-1}$ and $4.55 \times 10^{-5} \text{ cm}^2 \text{ s}^{-1}$ in LDH/PAA and (LDH/PAA)-CO₂, respectively. The MD simulations verify the adsorbed CO₂ decreases the diffusion of O₂ by viscous effects, which consequently cause the ultralow oxygen permeability of the (LDH/PAA)_{*n*}-CO₂ films. This result is consistent with the O₂TR test results (Figure 3A).

In summary, we demonstrate the fabrication of ordered films based on various XAl-LDH nanoplatelets (X = Mg, Ni, Zn and Co) and PAA by the LBL technique and subsequent CO₂ adsorption. The obtained (XAl-LDH/PAA)_{*n*}-CO₂ films with brick–mortar–sand structure display ultrahigh gas-barrier properties, which outperform most of the reported barrier materials. The impermeable LDH nanoplatelets impart a high resistance to the passage of oxygen molecules. Moreover, the adsorbed CO₂ as “sand” fills the free space in the LDH/PAA interface, which further decreases the diffusion of oxygen molecules. In addition, the (XAl-LDH/PAA)_{*n*} films can also inhibit the permeation of CO₂ and even of the smaller helium molecule. The strategy presented herein provides new insights into the understanding of the barrier mechanism, which in turn can be employed to fabricate ultrahigh-gas-barrier materials for use in a broad area including food and pharmaceuticals packaging, flexible electronic devices, and even gas separation and purification.

Keywords: brick–mortar–sand structures · carbon dioxide · free volume · gas barrier · layered double hydroxides

How to cite: *Angew. Chem. Int. Ed.* **2015**, *54*, 9673–9678
Angew. Chem. **2015**, *127*, 9809–9814

- [1] a) T. Kim, J. H. Kang, S. J. Yang, S. J. Sung, Y. S. Kim, C. R. Park, *Energy Environ. Sci.* **2014**, *7*, 3403–3411; b) C. Lu, Y. Mai, *Compos. Sci. Technol.* **2007**, *67*, 2895–2902.
[2] a) S. Seethamraju, P. Ramamurthy, G. Madras, *RSC Adv.* **2013**, *3*, 12831–12838; b) K. Jung, J. Bae, S. Park, S. Yoo, B. Bae, *J. Mater. Chem.* **2011**, *21*, 1977–1983.

- [3] S. Kim, S. Cha, *J. Appl. Polym. Sci.* **2014**, *131*, 40289–40296.
- [4] a) M. W. Möller, D. A. Kunz, T. Lunkenbein, S. Sommer, A. Nennemann, J. Breu, *Adv. Mater.* **2012**, *24*, 2142–2147; b) L. Introzzi, T. Blomfeldt, S. Trabatttoni, S. Tavazzi, N. Santo, A. Schiraldi, L. Piergiovanni, S. Farris, *Langmuir* **2012**, *28*, 11206–11214.
- [5] a) D. A. Hagen, C. Box, S. Greenlee, F. Xiang, O. Regev, J. C. Grunlan, *RSC Adv.* **2014**, *4*, 18354–18359; b) O. C. Compton, S. Kim, C. Pierre, J. M. Torkelson, S. T. Nguyen, *Adv. Mater.* **2010**, *22*, 4759–4763.
- [6] a) M. W. Möller, T. Lunkenbein, H. Kalo, M. Schieder, D. A. Kunz, J. Breu, *Adv. Mater.* **2010**, *22*, 5245–5249; b) D. A. Hagen, B. Foster, B. Stevens, J. C. Grunlan, *ACS Macro Lett.* **2014**, *3*, 663–666.
- [7] a) C. Wu, Q. Yang, M. Takeuchi, T. Saito, A. Isogai, *Nanoscale* **2014**, *6*, 392–399; b) M. A. Priolo, D. Gamboa, K. M. Holder, J. C. Grunlan, *Nano Lett.* **2010**, *10*, 4970–4974.
- [8] a) R. Nair, H. Wu, P. Jayaram, I. Grigorieva, A. Geim, *Science* **2012**, *335*, 442–444; b) R. Joshi, P. Carbone, F. Wang, V. Kravets, Y. Su, I. Grigorieva, H. Wu, A. Geim, R. Nair, *Science* **2014**, *343*, 752–754.
- [9] L. E. Nielsen, *J. Macromol. Sci. Rev. Macromol. Chem.* **1967**, *1*, 929–942.
- [10] a) W. R. Falla, M. Mulski, E. L. Cussler, *J. Membr. Sci.* **1996**, *119*, 129–138; b) E. L. Cussler, S. E. Hughes, W. J. Ward, R. Aris, *J. Membr. Sci.* **1988**, *38*, 161–174.
- [11] A. Ammala, S. J. Pas, K. A. Lawrence, R. Stark, R. I. Webb, A. J. Hill, *J. Mater. Chem.* **2008**, *18*, 911–916.
- [12] a) Q. Cheng, M. Wu, M. Li, L. Jiang, Z. Tang, *Angew. Chem. Int. Ed.* **2013**, *52*, 3750–3755; *Angew. Chem.* **2013**, *125*, 3838–3843; b) P. Podsiadlo, A. Kaushik, E. Arruda, A. Waas, B. Shim, J. Xu, H. Nandivada, B. Pumplun, J. Lahann, A. Ramamoorthy, N. Kotov, *Science* **2007**, *318*, 80–83.
- [13] a) Z. Xu, H. Sun, X. Zhao, C. Gao, *Adv. Mater.* **2013**, *25*, 188–193; b) H. Cong, P. Wang, S. Yu, *Chem. Mater.* **2013**, *25*, 3357–3362.
- [14] a) Q. Wang, D. O'Hare, *Chem. Rev.* **2012**, *112*, 4124–4155; b) H. Yao, H. Fang, Z. Tan, L. Wu, S. Yu, *Angew. Chem. Int. Ed.* **2010**, *49*, 2140–2145; *Angew. Chem.* **2010**, *122*, 2186–2191; c) F. Leroux, C. Taviot-Guého, *J. Mater. Chem.* **2005**, *15*, 3628–3642; d) R. Ma, K. Takada, K. Fukuda, N. Iyi, Y. Bando, T. Sasaki, *Angew. Chem. Int. Ed.* **2008**, *47*, 86–89; *Angew. Chem.* **2008**, *120*, 92–95.
- [15] a) L. Li, Y. Feng, Y. Li, W. Zhao, J. Shi, *Angew. Chem. Int. Ed.* **2009**, *48*, 5888–5892; *Angew. Chem.* **2009**, *121*, 6002–6006; b) G. R. Williams, D. O'Hare, *J. Mater. Chem.* **2006**, *16*, 3065–3074; c) M. C. Richardson, P. S. Braterman, *J. Phys. Chem. C* **2007**, *111*, 4209–4215.
- [16] a) J. L. Gunjekar, T. W. Kim, H. N. Kim, I. Y. Kim, S. J. Hwang, *J. Am. Chem. Soc.* **2011**, *133*, 14998–15007; b) F. Zhang, L. Zhao, H. Chen, S. Xu, D. G. Evans, X. Duan, *Angew. Chem. Int. Ed.* **2008**, *47*, 2466–2469; *Angew. Chem.* **2008**, *120*, 2500–2503.
- [17] a) J. L. Gunjekar, I. Y. Kim, J. M. Lee, N. S. Lee, S. J. Hwang, *Energy Environ. Sci.* **2013**, *6*, 1008–1017; b) J. W. Bocclair, P. S. Braterman, *Chem. Mater.* **1999**, *11*, 298–302; c) M.-Q. Zhao, Q. Zhang, J.-Q. Huang, F. Wei, *Adv. Funct. Mater.* **2012**, *22*, 675–694.
- [18] a) Y. Dou, S. Xu, X. Liu, H. Yan, M. Wei, D. G. Evans, X. Duan, *Adv. Funct. Mater.* **2014**, *24*, 514–521; b) D. Yan, J. Lu, M. Wei, J. Han, J. Ma, F. Li, D. G. Evans, X. Duan, *Angew. Chem. Int. Ed.* **2009**, *48*, 3073–3076; *Angew. Chem.* **2009**, *121*, 3119–3122; c) J. Han, Y. Dou, D. Yan, J. Ma, M. Wei, D. G. Evans, X. Duan, *Chem. Commun.* **2011**, *47*, 5274–5276.
- [19] a) Y. Dou, A. Zhou, T. Pan, J. Han, M. Wei, D. G. Evans, X. Duan, *Chem. Commun.* **2014**, *50*, 7136–7138; b) D. Yan, J. Lu, J. Ma, S. Qin, M. Wei, D. G. Evans, X. Duan, *Angew. Chem. Int. Ed.* **2011**, *50*, 7037–7040; *Angew. Chem.* **2011**, *123*, 7175–7178.
- [20] Z. Sun, L. Jin, S. He, Y. Zhao, M. Wei, D. G. Evans, X. Duan, *Green Chem.* **2012**, *14*, 1909–1916.
- [21] H. Du, C. Williams, A. Ebner, J. Ritter, *Chem. Mater.* **2010**, *22*, 3519–3526.
- [22] J. Han, Y. Dou, M. Wei, D. G. Evans, X. Duan, *Angew. Chem. Int. Ed.* **2010**, *49*, 2171–2174; *Angew. Chem.* **2010**, *122*, 2217–2220.
- [23] Y. Zhao, F. Li, R. Zhang, D. G. Evans, X. Duan, *Chem. Mater.* **2002**, *14*, 4286–4291.
- [24] R. Philipp, K. Fujimoto, *J. Phys. Chem.* **1992**, *96*, 9035–9038.
- [25] J. I. Di Cosimo, V. K. Díez, M. Xu, E. Iglesia, C. R. Apesteguía, *J. Catal.* **1998**, *178*, 499–510.
- [26] a) F. Carosio, S. Colonna, A. Fina, G. Rydzek, J. Hemmerlé, L. Jerry, P. Schaaf, F. Boulmedais, *Chem. Mater.* **2014**, *26*, 5459–5466; b) G. Findenig, S. Leimgruber, R. Kargl, S. Spirk, K. Stana-Kleinschek, V. Ribitsch, *ACS Appl. Mater. Interfaces* **2012**, *4*, 3199–3206; c) M. A. Priolo, K. M. Holder, D. Gamboa, J. C. Grunlan, *Langmuir* **2011**, *27*, 12106–12114.
- [27] a) D. Hagen, L. Saucier, J. Grunlan, *ACS Appl. Mater. Interfaces* **2014**, *6*, 22914–22919; b) J. Chen, Y. Fu, Q. An, S. Lo, S. Huang, W. Hung, C. Hu, K. Lee, J. Lai, *Nanoscale* **2013**, *5*, 9081–9088.
- [28] K. Liao, H. Chen, S. Awad, J. Yuan, W. Hung, K. Lee, J. Lai, C. Hu, Y. Jean, *Macromolecules* **2011**, *44*, 6818–6826.

Received: April 25, 2015

Published online: June 25, 2015